HHS Public Access

Author manuscript

Nat Biomed Eng. Author manuscript; available in PMC 2018 May 01.

Published in final edited form as:

Nat Biomed Eng. 2017 November ; 1(11): 914–924. doi:10.1038/s41551-017-0152-3.

Non-destructive two-photon excited fluorescence imaging identifies early nodules in calcific aortic-valve disease

Lauren M. Baugh[1], **Zhiyi Liu**[1], **Kyle P. Quinn**[1,2], **Sam Osseiran**[3,4], **Conor L. Evans**[3], **Gordon S. Huggins**[5], **Philip W. Hinds**[6], **Lauren D. Black**[1,6,†], and **Irene Georgakoudi**[1,†]

[1]Department of Biomedical Engineering, Tufts University, Medford, MA, 02155, USA

[2]Department of Biomedical Engineering, University of Arkansas, Fayetteville, AR, 72701, USA

[3]Wellman Center for Photomedicine, Harvard Medical School, Massachusetts General Hospital, Charlestown, MA, 02129, USA

[4]Harvard-MIT Division of Health Sciences and Technology, Massachusetts Institute of Technology, Cambridge, MA, 02139, USA

[5]Molecular Cardiology Research Center, Tufts Medical Center and Tufts University Sackler School for Graduate Biomedical Sciences, Boston, MA 02111, USA

[6]Cellular, Molecular, and Developmental Biology Program, Sackler School for Graduate Biomedical Sciences, Tufts University School of Medicine, Boston, MA 02111, USA

Abstract

Calcifications occur during the development of healthy bone, and at the onset of calcific aortic-valve disease (CAVD) and many other pathologies. Although the mechanisms regulating early calcium deposition are not fully understood, they may provide targets for new treatments and for

[†]**Correspondence should be addressed to:** L.D.B. (lauren.black@tufts.edu) or I.G (irene.georgakoudi@tufts.edu), Department of Biomedical Engineering, Tufts University, 4 Colby Street, Medford, MA 02155, Fax: 617-627-3231, Phone: 617-627-4353.

Data Availability

The authors declare that all data supporting the findings of this study are available within the paper and its supplementary information, source data for the figures in this study are available from the authors upon request.

Code Availability

Custom Matlab code used to calculate the relative MAF contributions is available for download through the following link: github.com/liuzhiyi16/MAF-code.

Author Contributions

L.B contributed to the conception and design of the experiments, collection and assembly of data, data analysis and interpretation, manuscript writing, and the final approval of manuscript. K.P.Q. performed data analysis and data interpretation, contributed to manuscript writing and final approval, and provided financial support (NIH-NIBIB Award # K99EB017723 and R00EB017723). Z.L. developed the computational model to extract quantitatively the component contributions from the images acquired at two emission bands and performed the corresponding calculations for both the human CAVD valves and the mouse model valves. Both G.H. and P.H. contributed to the data interpretation and final approval of the manuscript and, along with L.D.B., contributed financially (NIH – NHLBI Award # R01HL114794). S.O. and C.L.E. performed CARS and TPEF imaging as well as data interpretation of human CAVD and rat bone samples. G.H. also provided the human CAVD valve samples. I.G. directed the image acquisition and image analysis aspects of the study. L.D.B and I.G. contributed to the project conception and design, manuscript writing, data interpretation, and final approval of manuscript. I.G. also contributed financially via a NIH-NIBIB award (Award # R01EB007542) and the American Cancer Society Research Scholar Grant RSG-09-174-01-CCE.

Disclosures

None.

Competing Financial Interests

None.

early interventions. Here, we show that two-photon excited fluorescence (TPEF) can provide quantitative and sensitive readouts of calcific nodule formation, in particular in the context of CAVD. Specifically, by means of the decomposition of TPEF spectral images from excised human CAVD valves and from rat bone prior to and following demineralization, as well as from calcific nodules formed within engineered gels, we identified an endogenous fluorophore that correlates with the level of mineralization in the samples. We then developed a ratiometric imaging approach that provides a quantitative readout of the presence of mineral deposits in early calcifications. TPEF should enable non-destructive, high-resolution imaging of three-dimensional tissue specimens for the assessment of the presence of calcification.

Calcific aortic valve disease (CAVD) is characterized by a progressive thickening of the aortic valve leaflets and subsequent calcific nodule growth.[1] Currently, over 450,000 people in the United States, ages 65–74, have CAVD with aortic stenosis (AS);[2] many will require valve replacement surgery to prevent heart failure. Unfortunately, the primary method of diagnosis by echocardiography is only effective when AS is present in the valve,[3] which is frequently at advanced stages of the disease.[4] Given the significant mortality and morbidity associated with cardiovascular procedures in the elderly, the development of new non-surgical treatment methods (e.g. pharmaceuticals) for CAVD is of critical importance; however a more thorough understanding of the mechanisms associated with CAVD development is required. Current studies on CAVD mechanisms are limited to observations of either end-stage diseased valves, genetic mouse models that may not accurately describe human disease pathology, or *in vitro* model systems that induce calcification in conditions that attempt to mimic the *in vivo* disease.[4,5] Even in the latter two cases, where nodule formation and growth can be observed experimentally, quantification of calcification relies on destructive assays with finite spatial resolution that do not permit serial imaging of the same sample. The ability to study early calcifications with a non-destructive, high (micron-level) resolution method may help elucidate key mechanisms in the beginning stages of the disease, and factors influencing the propensity for disease progression. Such knowledge could have a significant impact on the development and assessment of critically needed interventions.

Current imaging methods used to study and diagnose CAVD include computed tomography (CT),[6] ultrasound,[7] magnetic resonance imaging (MRI),[8] molecular imaging with fluorochromes,[9] and second harmonic generation (SHG) imaging.[10–12] The use of positron-emission tomography can provide information on relevant biological processes *in vivo*, such as measuring both inflammation and active calcification in CAVD patients as a predictor of disease progression,[13] through the use of radioisotopes. Recent studies have highlighted the use of ^{18}F sodium fluoride (NaF)[14] as a means to quantify calcifications in the valves and predicting areas of calcification that could later be identified with CT.[15] Despite such promising results, the resolution of this imaging approach is approximately 4–5 mm,[16] which limits its ability to detect the presence of micron scale nodules. Further, the uptake of the ^{18}F NaF is reliant on actively calcifying cells, decreasing its ability to assess less dynamic calcifications in the valve.[14] Additionally, while electron beam CT imaging can provide high resolution images (0.24–0.33 mm for bone in humans[17]) with dual-scan contrast agents,[18] this modality still carries the risk of radiation exposure.[19] Molecular

imaging in the near-infrared region (700 nm to 1000 nm) has also been utilized in *in vivo* models to measure inflammation and bone mineralization,[20] but always with the use of exogenous chromophores,[9,21] adding complication and expense to the procedure. Non-destructive echocardiograms and MRI are limited by their spatial resolution (about 0.5 mm).[9,17,22] SHG imaging, which collects signals emitted from non-centrosymmetric structures, such as collagen fibers, has been a powerful tool for characterizing collagen fiber alignment and structure in tissue engineered viable heart valves,[10] and *ex vivo* animal or human heart valve tissue.[11,12] A recent study reported that CAVD was associated with layer-specific alterations in collagen architecture.[23] They used SHG imaging to quantify organizational changes of collagen fibers in human CAVD valves versus healthy ones, and found that the majority of changes in CAVD, including the fiber number, width, density and alignment, occurred in the layer of spongiosa, in contrast to relatively few changes in the layer of fibrosa.[23] However, using SHG imaging solely was not sufficient to provide a thorough understanding of mineralization, an important hallmark of CAVD. While many advances in imaging have been developed, all of these fail to fully describe microscopic morphological and functional changes within the valve tissue during CAVD development or to detect the early presence of calcification in a non-destructive manner. Interestingly, a recent study of human valve tissue found that many individuals classified as “healthy” can have microcalcifications (about 100nm to 5μm in size) present on their aortic valve leaflets; it was hypothesized that these tiny calcifications could develop into full aortic stenosis from CAVD and that understanding growth of these nodules may lead to clearer understanding of CAVD progression.[24] The study, which relied on *ex vivo* scanning electron microscopy (SEM) and transmission electron microscopy (TEM) to gain the resolution necessary for imaging the microcalcifications, highlights the need for an imaging modality that does not damage the sample so that these nodules can be observed within the context of living tissues and intact extracellular matrix to elucidate potential mechanistic pathways of CAVD progression.

In contrast to the above-mentioned imaging modalities, nonlinear, multiphoton optical microscopy is a non-destructive, micron-scale resolution imaging approach with intrinsic depth sectioning that has been used extensively to image a variety of tissues.[25,26] Specifically, two-photon excited fluorescence (TPEF) utilizes near-infrared light (NIR) to excite endogenous tissue fluorophores with emission in the visible range.[26–28] For example, TPEF has been used to quantify elastin and collagen in mouse valve tissue[29] and used to assess the state of tissue engineered heart valves.[30] Other studies have indicated the presence of single-photon excited autofluorescence from calcified tissue in the 515 nm emission regime, although this signal was never fully quantified.[31] This suggests that TPEF could be used to image calcifications in a non-destructive manner within the context of fresh tissue samples. While this endogenous signal could also be exploited using standard fluorescence confocal imaging to acquire high 3D resolution assessments of calcifications, nonlinear microscopy enables such measurements over more extended depths and is less susceptible to photo-bleaching.[32,33] However, further characterization of this signal is necessary since other molecules, such as collagen, also autofluoresce in this wavelength range.[34] The distinction of mineralization associated fluorescence (MAF) from that of collagen is potentially easier using non-linear instead of linear interactions in two respects: a) for reasons that are not clearly understood the TPEF cross-section of collagen is relatively low

compared to its single-photon excited fluorescence cross-section,[35] and b) SHG signal of collagen fibers can be easily collected at the same time as TPEF to identify their location with high specificity.[36] In fact, the acquisition of co-registered TPEF and SHG images for the study of calcifications in the context of extracellular matrix remodeling is one of the leading advantages of non-linear microscopic imaging compared to more established modalities such as CT and PET. In this study, we acquired TPEF spectral images from a range of calcified samples, including excised valves from human CAVD patients, rat bone fragments, and calcific nodules generated *in vitro* using polyacrylamide (PAAM) gels to identify endogenous TPEF readouts of calcification. Examination of spectral differences enabled us to identify two components, one attributed to collagen, the second to mineralization associated fluorescence (MAF). Further analysis, led to a simple, yet quantitative imaging scheme optimized to highlight regions rich in calcified deposits. Thus, our results indicate that TPEF imaging may provide a new tool to non-destructively quantify mineralization with high sensitivity and spatial resolution during CAVD progression.

Results

Comparison of Imaging Techniques for Calcification

To assess the potential of detecting mineralized deposits using TPEF, we compared multiphoton images with histological images of the commonly utilized calcification stain Alizarin Red. Representative endogenous TPEF images acquired with 800nm excitation and at 525 ± 25 nm emission from human CAVD patient valves, from rat tibia bone samples, and from calcified nodules grown *in vitro* using PAAM-collagen gels were compared with corresponding images acquired from the same samples after Alizarin Red staining (Figure 1). The endogenous TPEF signal patterns are generally consistent with those of the stain, suggesting that mineralized deposits exhibit enhanced TPEF in this spectral region. The similarities observed are remarkable given that the Alizarin Red stained images are transmission images, relying on absorption contrast from the entire tissue sample, while the TPEF images represent either single optical sections or 3D projections of a 315 μm thick TPEF stack for the human CAVD nodule, a 110 μm thick TPEF stack of rat bone, or a 265 μm thick TPEF stack of the PAAM gel nodule. The intensities of TPEF and Alizarin Red images of CAVD, bone, and PAAM gel nodules are significantly correlated, further supporting that the enhanced TPEF signal in these images is associated with the levels of mineralization (Supp. Figure 1A, R^2=0.7334, p=0.0002).

To illustrate the capability of TPEF imaging capability to highlight fine structural mineralization features, such as ridge edges and surface roughness, CAVD valves, rat bone tibia, and PAAM gel nodules were imaged using SEM and TPEF. Structural similarities are observed between representative SEM images and TPEF optical sections and 3D projections. The human CAVD nodule, rat bone, and PAAM gel nodule 3D reconstructions are composed of images from a 160 μm thick, a 115 μm thick, and a 147 μm thick TPEF stack, respectively (Figure 2). The sections demonstrate that the TPEF signal is not limited to superficial features. Thus, unlike SEM imaging, TPEF images provide structural details of the mineralized deposits throughout their imaged volume. Further, texture analysis of the SEM and TPEF images taken from CAVD valves and bone reveals that the organization

features of the two types of images are strongly correlated (Supp. Figure 1B; R^2=0.8157, p=0.002). Thus, these comparisons indicate that endogenous TPEF images provide useful information regarding mineralization content and organization that are typically acquired using invasive microscopic imaging procedures.

Spectral Analysis of Mineralized Tissue

Collagen is abundant in valve tissue and is the primary component of the fibrosa layer of the aortic valve, the region of the leaflet where the majority of calcifications begin.[1] Collagen fibers are strong sources of a nonlinear (two-photon) scattering process, referred to as second harmonic generation (SHG), because of their non-centrosymmetric structure[37]. SHG has been used extensively to assess collagen fiber organization and structure.[38–41] Additionally, TPEF and SHG imaging can be performed simultaneously, and their combined use could enable assessment of calcific nodule formation in the context of collagen organization and remodeling. However, collagen fibers are also natural TPEF emitters, with the signal emanating primarily from collagen crosslinks.[42,43] Thus, in order to exploit TPEF as a sensitive biomarker of calcification, it is important to identify differences in its TPEF emission from that of collagen.

To gather further evidence that the TPEF signal detected in the 500–550 nm region originates primarily from calcified deposits within the samples, we acquired and compared images from CAVD and rat tibia bone tissue samples prior to and following treatment with EDTA, a known Ca^{2+} chelator.[44] Overlaid with the TPEF images (red) are corresponding SHG images (blue) acquired from the same field of view to demonstrate that the TPEF signal is not simply collagen autofluorescence (Figure 3). Specifically, we observe that the pattern of the bright TPEF signal is quite distinct from the SHG producing collagen fibers, and the prevalence of the TPEF signal decreases upon EDTA treatment for both the CAVD and bone samples. We do not detect any SHG signal in the PAAM gels, since they consist of disorganized, solubilized collagen. Representative TPEF stacks from all imaged tissue types can be seen in Supp. Videos 1–6.

FT-IR spectra of bone and CAVD samples confirm the reduction of mineralization with EDTA treatment (Figure 3F). Specifically, a decrease in the phosphate peak (1000 cm^{-1} – 1200 cm^{-1}), which is an important hydroxyapatite component,[45] is seen with EDTA treatment in both sample types.

Previously, endogenous autofluorescence in the 450–700 nm range has been described as deriving from lipids,[31,46] elastin,[31,46] collagen,[46] and ceroid deposits[47] found in atherosclerotic plaques. In fact, single photon autofluorescence of calcifications has been reported in plaques collected using 515 nm and 610 nm barrier filters,[31] which is consistent with our mineralization associated TPEF signal. However, endogenous TPEF emission excited at 800 nm and detected at 520 ± 40 nm from calcified plaques has been attributed, at least partly, to lipids whose presence was confirmed by Coherent Anti-Stokes Raman Scattering (CARS) imaging.[48] Careful inspection of the images of that study indicates that there was additional autofluorescence signal surrounding the CARS-identified lipid, which could have been originating from within the mineralized deposit, but this possibility was not explored.

To better understand and characterize the origins of the observed TPEF signal in our samples, we collected full spectral images; i.e. we gathered forty TPEF images, each representing the signal over a 20 nm bandwidth in the 400 to 700 nm range and centered approximately 7 nm apart from each other (Supp. Figure 2). Thus, each pixel contained a full TPEF emission spectrum. The mean spectra collected from each sample type are shown in Figure 4 A–C, along with the corresponding fits to these spectra resulting from non-negative linear factorization analysis, which revealed major contributions from two components (Figure 4D). The two-component model provided a good fit to the spectra of each sample group (human CAVD valves: R^2=0.997 ± 0.006, rat bone specimens: R^2=0.973 ± 0.034, and PAAM gel specimens: R^2=0.990 ± 0.005). The first component has an emission peak at approximately 480 nm, which is consistent with collagen TPEF excited at 800 nm[42]. The second component is associated with the mineralized deposits, as indicated by: a) the significant decrease in the relative contribution of this component upon EDTA treatment with the CAVD and tibia bone specimens ($p=0.088$ for CAVD and $p<0.001$ for tibia bone samples; Figure 4E), and b) its almost exclusive (93 ± 6%) contribution to the TPEF emission collected from the nodules grown on PAAM gels, which aren't expected to have any collagen-associated TPEF.[49] Similar spectral components were produced at 860 nm excitation (Supp. Figure 3). Notably, the spectra for the MAF component are nearly identical for both excitation wavelengths, with a peak at approximately 530 nm. On the other hand, the peak for the collagen-associated TPEF component had a slight red shift, which has been reported previously for collagen emission.[42] Additionally, the detected 525 nm signal attributed to mineral deposits is highly unlikely to emanate from lipids. End-stage human CAVD and tibia bone samples are heavily calcified and are expected to have minimal lipid content.[50] While the identity of the MAF component is not clearly recognized, the fact that its emission spectrum does not shift as a function of excitation wavelength, suggests that it is a single biochemical moiety. Since, we do not have a means of establishing the concentration of the MAF component, it is not possible to quantify its TPEF cross-section. However, we have made quantitative comparisons between the collagen and mineralization rich regions and have found the mean MAF TPEF intensity per pixel to be 2.5 ± 0.6 times higher the mean collagen TPEF intensity at 800 nm excitation. While the relative MAF TPEF intensity tended to be lower for the EDTA treated samples, there were no statistically significant differences in the mean MAF to collagen TPEF intensity ratio for any of the sample groups examined.

Using a Ratiometric Approach to Enable Rapid MAF Imaging

While preforming a full spectral analysis on a range of samples that are expected to have varying contributions from a set of fluorophores is an important first step in determining the spectral emission properties of these components, it is extremely time-consuming; this would be especially challenging in an *in vivo* setting and would require specialized instrumentation that could hinder the usability of this technique. However, quantifying the emission spectra of the two components and exploiting their differences, enabled us to develop a simple yet quantitative approach for extracting the relative contribution of the MAF component, relying on only two images (see Methods). These TPEF images are acquired at two distinct emission bands centered at 460 and 525 nm (shown as a highlighted regions on top of the two component spectra of Figure 4D). Representative overlays from

TPEF images in these two ranges along with the SHG image from the same field of view are shown in Figure 5A and C from CAVD samples prior to and following EDTA treatment. Images from the individual channels can be found in Supp. Figure 4. Corresponding processed images highlighting the extracted relative contribution of the MAF component (Figure 5B and D) demonstrate the ability of this approach to enhance visualization of mineral deposits. In addition to such qualitative visual assessments, we can extract quantitative, significant differences in the levels of the MAF upon EDTA treatment for both CAVD ($p=0.002$) and bone tissue samples ($p=0.045$; Figure 5E).

CARS Imaging Confirms Hydroxyapatite Origins of MAF Signal

As a further confirmation that the observed fluorescence is associated with mineralization, CARS imaging was performed on both CAVD valves and rat bone to look for evidence of hydroxyapatite formation. CARS is a parametric nonlinear optical imaging technique where the contrast arises from the intrinsic vibrational modes of a given chemical group.[51] The 3570 cm^{-1} vibrational band of OH^- in hydroxyapatite was imaged using CARS microscopy and overlaid with the calculated MAF images for both the valve and bone samples (Figure 6), showing a strong correlation between MAF and CARS samples. The strong overlap between the CARS and MAF signals indicates the MAF signal is likely emanating from hydroxyapatite in the valve.

Applying the Ratiometric Method to ApoE−/− Mouse Model

To demonstrate that the optical imaging approach we developed to detect and monitor valve mineralization in a quantitative and sensitive manner is applicable to a wide range of samples that are relevant to tissue calcification, we used the same image acquisition and analysis protocol to assess the relative MAF contributions within freshly excised valves acquired either from WT or ApoE−/− mice, which were fed a high fat diet to increase valve mineralization. This mouse model is the most frequently used animal model of CAVD disease and has played an important role in identifying mechanisms relevant to CAVD development and treatment.[52,53] While there are limitations to using a genetic mouse model to study CAVD, several studies have shown that they are an adequate platform for studying the underlying osteogenic pathways associated with CAVD, even if they have fallen short in the transition to clinical trials.[54] In particular, ApoE−/− mice exhibit upregulation of many osteogenic markers and form lesions that express bone makers such as ALP, Runx2, and osteocalcin.[55] In our study, we simply exploit the previously documented formation of mineral deposits in the valves of these mice as an example of preclinical studies in which our approach can be used to detect the level of mineralization. Spectral image analysis confirmed that the collagen and MAF components described the TPEF emission recorded from these samples well ($R^2=0.976 \pm 0.005$ for the ApoE−/− mouse valves and $R^2=0.981 \pm 0.010$ for WT mouse valves). Another fluorescent component may be present in these tissues in the 650–700 nm region, but that is clearly distinct from the signals we detect in the 460 and 525 nm regions of the spectrum which are fit with high accuracy by the two-component model (Supp. Figure 3). Thus, TPEF images were taken using the same protocol as the one used for our previous samples. Overlays of the collected images are shown with the corresponding processed images that highlight the relative prevalence of the MAF component in the different tissue samples in Figure 7. Images used for the overlays are

included in Supp. Figure 5. An increase in the MAF component is immediately evident within the ApoE−/− mouse valves upon visual inspection of the images (Figure 7 B, D). Quantitative evaluation of these images reveals indeed a significant increase in the relative MAF contribution from the WT to the ApoE−/− mice (p=0.0525; Figure 7E).

Time Lapse Imaging Tracks Nodule Growth

To demonstrate the sensitivity and potential of the described MAF-based method to track mineral deposition from its onset, we monitored the growth of calcific nodules in a PAAM gel system seeded with valve interstitial cells (VICs) over 5 days. The PAAM gel was imaged every 8 hours for 120 hours (Supp. Video 7) and the growth of individual nodules was assessed. For each time point, the 460 and 525 nm TPEF images were processed to generate a stack of images of the relative MAF contribution. This stack was then integrated in the Z direction to yield a 2D projection at each time point (Figure 8A shows the projection at the start of the experiment). Images from each time point are stacked and regions of interest (ROIs) are cropped from the entire image stack. Four ROIs from this projected image were analyzed for nodule growth as shown in Figure 8A and B, time lapse videos in Supp. Video 8–11, and representative images of a single ROI in Supp. Figure 6A (see Supp. Figure 6B for additional detail of the method). A representative image of the summed slices of one ROI is shown in Figure 8C, while Figure 8D shows the respective line plots of the intensities of Figure 8C. The line plots were generated by integrating each ROI along the × direction; we generated one dimensional plots characterizing the nodule MAF intensity at each time point. The FWHM of these plots are associated with the cross-sectional width of the nodules (Figure 8E) and their integral represents the nodule MAF volumetric intensity (Figure 8F), which is a measure of its overall mineral content. The calculated FWHM and the nodule volumetric intensity show nodule growth for all ROIs, except for ROI 3 which displays a decrease in volumetric intensity, though still an increase in nodule width.

Interestingly, nodule growth was not uniform with ROI 3 decreasing in size overall (based on the nodule volumetric intensity plot) even as it grew outwards along the PAAM gel (as shown by an increase in the FWHM). This exemplifies how nodule development may not be uniform within mineralized tissue and that active changes in calcification could add another layer of consideration to CAVD diagnosis. While the overall mineral content increased over the experimental time course, the MAF-based imaging method was able to detect small changes in the manner in which individual nodules grew. Understanding the dynamic changes that occur at calcification foci could be a key step in understanding the development of mineralization or their response to treatment.[56]

Discussion

The lack of clinical success in non-surgical treatment of CAVD highlights the need for improved understanding of the underlying disease mechanisms. Recent literature suggests that optical methods in particular could have a large impact on preclinical research.[9] Such methods offer the potential for imaging at high, micron-level resolution that may enable identification of CAVD lesions at the early stages of the disease, when therapy may be more

effective. In this study, we show that calcified nodules exhibit endogenous fluorescence signatures that can be exploited by TPEF imaging to enable non-destructive visualization of calcifications with micron-level resolution. Specifically, we find that endogenous TPEF with a peak emission at 530 nm is detected from mineral-rich specimen regions when excited at 800 or 860 nm. This emission is distinct from that of collagen crosslink TPEF, which, as expected, has a peak that becomes red-shifted as the excitation wavelength increases.[57]

The characterization of the detailed spectral emission profile of the MAF and its comparison to the emission from collagen fibers, which are typically present in mineralized samples, enabled us to develop a simple, and fast, yet robust approach to quantify the relative MAF contributions within a specimen. This method relies on the collection of two images centered at 460 and 525 nm upon excitation at 800 nm, which can be combined to provide a quantitative readout of the relative prevalence of the MAF. We validate the sensitivity of this approach by demonstrating that we detect a decrease in the relative MAF levels upon EDTA treatment of both human CAVD and rat tibia bone samples. We further confirm the biochemical origins of MAF using FT-IR and co-registered CARS and TPEF measurements. To demonstrate that this simple imaging protocol is relevant to the analysis of a broad range of specimens, we apply it to the characterization of valve samples from wild type and ApoE −/− mice, a widely used animal model for CAVD studies.[58] Analysis of these samples further validates the sensitivity of this optical imaging scheme to the enhanced levels of mineral deposits that are formed in the knockout mice valves.[58] While there are clearly limitations in terms of the clinical relevance of the ApoE−/− mouse model of CAVD, our approach should be applicable and potentially very useful in assessing CAVD progression in emerging pre-clinical disease models. These include *in vitro* models of calcification[59] and new genetic mouse models of CAVD.[60] In addition to potential *in vivo* imaging strategies in animal models, we showed that MAF quantification can be used to track nodule growth, non-invasively, over time in *in vitro* conditions. Nodules smaller than 10 microns in their cross-sectional width were imaged and showed growth overtime which we tracked in all three spatial dimensions over time.

Given the micron-level resolution of TPEF imaging, the approach we describe bears great promise as a tool that may be used to detect and monitor dynamically the development of mineralized deposits from a very early stage using pre-clinical CAVD models. Such advances are expected to have a significant impact on our understanding of the disease and the development of more effective treatments. While advances in micro-CT/PET imaging methods have led to better predictive capabilities of CAVD progression in patients, more could be learned with a better understanding of ECM changes and mineralization at a cellular level within the valve. NIR imaging techniques that use dyes to visualize the development of mineralization are able to detect small ossification before even high resolution micro-CT, which provides an even better understanding of calcification development.[61] Direct clinical translation of TPEF imaging to monitor CAVD may be initially complicated by the need to perform such measurements through millimeter sized endoscopes. Such multiphoton endoscopes are not immediately available for intravascular use, but we expect that continuous advances in probe development and human in vivo TPEF measurements will ultimately make such measurements a real possibility.[62,63] Currently, the 2014 American Heart Association/American College of Cardiology guidelines recommend

the use of cardiac catheterization to measure blood hemodynamics for patients that cannot be diagnosed through echocardiographic imaging[64]; the use of an imaging probe either in place of or in conjunction with a catheter is therefore a reasonable goal. Additionally, because of the increased resolution capabilities of capturing MAF over current imaging modalities, high risk patients such as those with a bicuspid aortic valve,[65] could be imaged to look for potential CAVD mechanisms early in the disease process. MAF could also be used with CT/PET imaging methods on patients testing positive for CAVD to look for smaller nodules within the context of ECM changes. The development of single-photon excitation-based measurements of MAF are also possible, because in most cases the single and two-photon excited fluorescence emission spectra of molecules are highly overlapping. A number of optical probes have been used for intravascular imaging using different modalities, such as optical coherence tomography (OCT), photoacoustics, and fluorescence, alone or in combination.[66–68] In addition, confocal microendoscopy probes as small as 0.6 mm in diameter have already been developed.[69] Thus, an endogenous fluorescence-based high-resolution imaging system developed and optimized for mineral deposition detection in human valves is technologically highly feasible. Of course, thorough studies that establish the sensitivity and specificity of this approach will be needed. Finally, we should note that such a probe may also be more broadly applicable for the detection, characterization or monitoring of other conditions affected by the presence of calcifications, including atherosclerotic plaques[70] and breast cancer.[71] While direct translation of this approach to the clinic will require addressing significant challenges associated with miniature probe development and minimizing the optical impact of blood, its relevance to more fundamental studies with *in vitro* and *ex vivo* tissues to improve our understanding of the disease is immediate.

Methods

All animal experiments were approved by the Institutional Animal Care and Use Committee at Tufts University and performed in agreement with Tufts University guidelines and the US Animal Welfare Act. Human samples of valves taken from patients undergoing replacement surgery for advanced CAVD were acquired under a protocol approved by the Tufts University School of Medicine Institutional Review Board (IRB number 10273). The tissues were considered discarded tissues (not removed for research purposes) and obtained only with patient consent.

Human CAVD Valve Samples

All male patients were used; ages ranged from 56–72 years. Within 24 hours of extraction, samples were frozen to −80°C until imaging. Eight samples were acquired for this study.

Rat Valve Interstitial Cell (VIC) and Bone Isolation and Culture

Aortic valve leaflets were surgically removed from Sprague Dawley rats within 30 minutes of euthanasia and used to isolate VICs for the formation of calcified nodules *in vitro*. The valve leaflets were placed in a 12 well plate with standard culture media [Dublecco's Modified Eagle's Medium (DMEM; ThermoFisher Scientitfic, Waltham, MA [10566016]), 1% Fungizone (ThermoFisher Scientific, Waltham, MA, Antibiotic-Antimycotic

[15240062]), and 10% fetal bovine serum (FBS, ThermoFisher Scientific, Waltham, MA [16000-044])]. Tissue samples were placed in an incubator at 37°C with 5% CO_2 for 10 days, with media changed every 2–3 days. Cells were allowed to migrate out of the tissue and adhere to the plate. VICs isolated in this manner were passaged and expanded in traditional culture flasks in standard culture medium. VICs that had been passaged 2–6 times were used for experimentation.

Male Sprague Dawley rat tibia bones were also isolated from sacrificed animals. Skin and muscle tissue were removed from the hind leg of three rats with a scalpel and 5 × 5 mm bone sections were removed from the tibia. Samples were washed and stored in 1X PBS for less than a week before imaging or fixation.

Polyacrylamide (PAAM) Gel Preparation

Before the creation of PAMM gels, 22 mm × 22 mm glass cover slips were activated to create binding sites as previously described.[49] To increase hydrophilicity, cover slips were passed through an open flame and then covered with 0.1M NaOH (Millipore, Billerica, MA [SX0607H-3]). After the slips dried, 3-aminopropyltrimethoxy was smeared onto the cover slips and allowed to dry. Slips were then placed into 6-well plates and washed three times in diH_2O using an orbital shaker before being smeared with 0.5% glutaraldehyde (Sigma-Aldrich, St. Louis, MO [E6758]) and allowed to set for 30 minutes. After aspirating off the glutaraldehyde, the slips were again washed in diH_2O three times for five minutes. Activated cover slips were stored in diH_20 at 4°C until use.

To create the PAAM gels, acrylamide and bis- acrylamide were combined with 400 μg of rat tail collagen (ThermoFisher Scientific, Waltham, MA [A1048301]) and acrylic-acid-N-hydroxysuccinimide (NHS; Sigma-Aldrich, St. Louis, MO [A8060-1G]) ester (used to create covalent linkages between amine groups on the collagen and the PAAM gel). 1 N HCl was added to the solution to lower the pH to 6.8–6.9 before acrylamide to bis-acrylamide cross-linking was initiated using tetramethylethylenediamine (TEMED; Sigma-Aldrich, St. Louis, MO [411019]) and 10% ammonium persulfate (APS; Sigma-Aldrich, St. Louis, MO [A3678]).[72] By altering the ratio of acrylamide to bis acrylamide, the PAAM gels were created to have a stiffness of 35 kPa to mimic CAVD mechanical physiology.[73] To create a stiffness of 35 kPa a solution containing 10% w/w acrylamide and 0.1% w/w bis acrylamide was used.

Activated cover slips were dried in a sterile cell culture hood and 80 μL of each gel solution was placed onto the cover slips. A non-activated cover slip was then placed directly onto the gel solution to reduce airflow and promote polymerization while creating an even gel surface. After 30–45 minutes, the top cover slip was removed from the polymerized gels using a razor blade. The gels were moved to sterile 6-well plates and washed three times for 5 minutes each with sterile 1X PBS (ThermoFisher Scientific, Waltham, MA [BP3994]).

Following creation of the PAAM gels, isolated VICs, were seeded at a density of 50,000 cells/gel and allowed to adhere to the gels for 24 hours before being moved to separate culture plates to avoid potential paracrine signaling from cells adhering to the tissue culture plastic during seeding. PAAM gels were dosed with 1.25 ng/mL TGF-β_1 (Peprotech, Rocky

Hill, NJ [100-21]) for 24 hours in an incubator at 37°C with 5% CO_2. After 24 hours, media was replaced with the standard culture media described above and the PAAM gels were allowed to develop nodules for 14 days; media was changed every 2–3 days.

Demineralization with EDTA

Following TPEF imaging, samples fixed with 4% paraformaldehyde (in order to maintain collagen structure) and placed in 0.02% w/v ethylene-diamine-tetra-acetic acid (EDTA; Sigma-Aldrich, St. Louis, MO [E6758]) on an orbital shaker at room temperature for three weeks for demineralization, as previously described.[44] The samples (4 human CAVD and 3 rat bone) were then washed with 1X PBS and imaged using both the Leica TCS SP2 and our custom laser scanning microscopes. Every attempt was made to acquire images from similar locations within the same samples before and after EDTA treatment.

Alizarin Red Staining

A 0.02% wt/v Alizarin Red (Sigma-Aldrich, St. Louis, MO [A5533]) solution (pH 4.2 with NaOH) was used to stain the PAAM gel nodules, bone samples and human CAVD valves after TPEF imaging. After fixation with 4% w/v paraformaldehyde (Sigma-Aldrich, St. Louis, MO [158127]) for 10 minutes and washing with 1×PBS, the PAAM gels were placed in to the Alizarin Red solutions for 45 minutes. The same procedure was followed for the bone and human sample, but with longer fixation (20 minutes) and staining (1.5 hours) times. All samples were then washed with diH_2O several times (until the wash water was clear at the end of the rinse; about 8–10×) before imaging using an Olympus FSX100 (Tokyo, Japan).

For comparison imaging of the same fields, small portions of each sample were fixed to a glass slide with a clear adhesive. The samples were first imaged using the Leica TCS SP2 microscope and the image locations were carefully noted. The slides were then stained with Alizarin Red as described above, and imaged a second time with the Olympus FSX100 with the same fields of view that were taken with the Leica microscope described below.

Intensity correlation analysis between TPEF and Alizarin Red staining images

In order to quantitatively compare the TPEF and Alizarin Red stained images, we assessed the correlation in the intensity of corresponding fields imaged by the two approaches. First, five-level Otsu intensity thresholding[74] was applied to both TPEF and Alizarin Red stained images corresponding to similar fields. The lowest level was designated as low intensity background noise, while regions assigned to the upper four quantized levels in TPEF or Alizarin stained images were used to define the tissue areas from which the mean intensities were calculated. Four CAVD samples, four bone samples and five PAAM samples were used for this intensity correlation analysis, which was carried out in Excel.

Scanning Electron Microscope Imaging

Samples were prepared by gold sputter coating and imaged using a Carl Zeiss (Jena, Germany) EVO MA10 scanning electron microscope.

Micro-Structure Correlation Analysis between TPEF and SEM images

In order to assess if TPEF images enable characterization of similar micro-structure features as SEM images, we used a Fourier-based analysis approach we developed previously.[75–78] Briefly, the image intensity patterns within the tissue regions, as determined by the Otsu intensity thresholding method described in the previous section, were cloned and randomly positioned in the image background to create a new image without distinct borders and only tissue patterns covering the entire field. Then, we acquired the power spectral density (PSD) of the two-dimensional Fourier transform of this image, which represents the level of autocorrelation of the intensity fluctuations within the image over a range of relevant spatial frequencies. This curve exhibited an inverse power law behavior, which was fit using an equation of the form $R(k) \sim k^{-\beta}$, where k is spatial frequency. The value of β depends on the texture features of the images and was determined for both TPEF and SEM images corresponding to the similar field of the same specimen from 4 CAVD samples and 4 bone samples. To image in the same region of each sample with both imaging modalities, small pieces of samples were glued to a glass slide so that each image location could be mapped during the TPEF imaging process and then found during SEM imaging. It was not possible to analyze PAAM gel samples in the same way because the dehydration prior to SEM imaging significantly alters the PAAM gel nodule structures. The correlation analysis was done in Excel.

Fourier Transform Infrared (FT-IR) Spectroscopy

Three rat tibia bones and four CAVD valves were split into two pieces of roughly the same size. The two groups of samples were placed on an orbital shaker, at 4°C, either in the 0.02% EDTA solution used to reduce mineralization or in standard 1× PBS. After 3 weeks on the shaker, the samples were dried for 4 hours in a VirTis Genesis 25L Super XL Freeze-Dryer (SP Scientific, Stone Ridge, NY) and measured using FT-IR [JASCO FTIR 6200 spectrometer (JASCO, Tokyo, Japan) equipped with a MIRacle™ attenuated total reflection (ATR) Ge crystal cell in reflection mode]. Spectra were taken between 600 cm^{-1} and 3400 cm^{-1} with 1cm^{-1} increments. A linear baseline was fit to the regions of the FTIR spectra devoid of significant absorbance peaks (1800 cm^{-1} to 2500 cm^{-1}) and subtracted from the spectra. The spectra were then normalized using the total area under the curve. The CAVD and EDTA CAVD spectra were then shifted up the y axis to more clearly show the two sample types. The standard error of the mean was also calculated and plotted for each group.

Two-Photon Excited Fluorescence Imaging

TPEF spectral images were taken on a Leica TCS SP2 (Wetzlar, Germany) confocal microscope equipped with a Ti:sapphire laser (Spectra Physics, Mountain View, CA) and a dry Leica 20×/0.7 NA objective. To obtain spectral emission data, the laser was tuned to either 800 nm or 860 nm and images were collected between 400 nm and 700 nm in 40 equal increments (7.2 nm steps), each with a bandwidth of 20 nm. Using the Rayleigh criterion, the computed lateral resolution for this objective is 0.697 μm and the axial resolution is 3.265 μm.3D image renderings were created using ImageJ (NIH, Bethesda, MA).

Fluorescence spectra from all tissues were decomposed in two components using a blind spectral unmixing algorithm. This data set included 6 spectra from human CAVD valves, 8 spectra from EDTA treated human CAVD valves, 7 spectra from rat bone, 5 spectra from EDTA treated rat bone, and 3 spectra from nodules grown on 35 kPa PAAM gels. Specifically, non-negative matrix factorization was performed through an alternating least squares algorithm using a modification of the nnmf.m function in MATLAB. A two component model was used with random initial guesses for component concentrations. To avoid convergence to a local minimum, factorization of the component spectra and their relative concentrations in each tissue was performed 1000 times and the solution providing the smallest norm of the residual was selected. A two component model was selected based on its ability to describe 99.46% of the variance in emission spectra data. The relative contribution of component 2 was calculated for each spectrum and the calculated average for each sample specimen was used for statistical analysis (4 CAVD valves, 3 rat bones, and 3 PAAM gel nodules).

The rat bone and the human CAVD valve samples were further imaged using a custom-built laser scanning multiphoton microscope, which enabled simultaneous image acquisition by three non-descanned detectors equipped with filters at 400 nm ± 10 nm (ET400/20X), 460 ± 20 nm (HQ460/40m-2p), and 525 ± 25 nm (ET525/50M-2P). TPEF and SHG images were acquired at 800nm excitation. A Leica 20×/0.7 NA objective was used for image acquisition of four human CAVD samples and three rat bone samples. For each sample, both before and after treatment with EDTA, 3 images were taken from three distinct regions on the sample. The calculated MAF values were averaged to give a single measurement for each biological replicate (4 for the human CAVD valve and 3 for the rat bone samples) for statistical analysis.

Image-Based Quantitative Assessment of Mineralization Associated Fluorescence (MAF)

Based on the spectra of the collagen and the MAF components extracted from the spectral decomposition described above, we developed a simple method to enable us to quantitatively extract the relative MAF contribution based on image acquisition at two distinct spectral bands: 460 nm ± 20 nm and 525 nm ± 25 nm. The TPEF image intensity at these two bandwidths can be expressed as:

$$I_{460}=\xi_{460}(\alpha_{460}C_1+\chi\beta_{460}C_2) \quad (1)$$

$$I_{525}=\xi_{525}(\alpha_{525}C_1+\chi\beta_{525}C_2) \quad (2)$$

where ξ_{460} and ξ_{525} are the quantum efficiencies of the detectors at 460 nm and 525 nm, and C_1 and C_2 are the concentration of component 1 and 2, respectively. α_{460} and α_{525} are the fluorescence yields of component 1 at 460 nm and 525 nm respectively, and β_{460} and c are those corresponding to component 2. χ is a factor accounting for the difference of fluorescence efficiency of the two components. According to equations (1) and (2), the formalism for the concentration ratio of these two components is as follows:

$$C = \frac{\xi\alpha_{460} - I\alpha_{525}}{\chi(I\beta_{525} - \xi\beta_{460})} \quad (3)$$

where $C = C_2/C_1$, $\xi = \xi_{460}/\xi_{525}$, and $I = I_{460}/I_{525}$. We obtain the α_{460}, α_{525}, β_{460} and β_{460} from the spectra of component 1 and 2, which are 0.3394, 0.3590, 0.0812 and 0.3614 respectively. The ξ value of 0.8573 is acquired based on TPEF images acquired from extracted pure rat tail collagen fibers using the same excitation/emission data acquisition settings, and the χ value of 0.1520 is acquired by the raw intensity images of the experimental samples. Since the I values corresponding to each sample are readily accessible, we obtain the C values specific to each sample, and, finally, the relative contribution of the MAF component, C_2 as $C_2/(C_1 + C_2)$, which in this form is a value that always varies between 0 and 1.

MAF TPEF Intensity Analysis

To assess the TPEF MAF intensity (800 nm excitation) relative to that of collagen, we extracted the TPEF intensity ratio within the mineralization-rich and collagen-rich regions from each field of all the CAVD and bone samples we examined. To identify the collagen-rich regions, we manually selected regions with strong SHG signal, such as the blue areas within the RGB images shown in Figure 5A, C). We then calculated the mean TPEF intensity within this region, which we attributed to collagen. To identify the mineralization-rich regions, we first acquired the MAF ratio map for each field, identified pixels with the top 10% MAF ratio values, and calculated the mean MAF TPEF intensity within each such region. Given the spectral characteristics of collagen and MAF TPEF relative to the bandpass or our 525 nm emission filter, we estimated the expected collagen and MAF TPEF intensity based on the full spectral emission of each component. In this manner, we acquired for each field an intensity ratio representing the MAF TPEF intensity relative to that of collagen. As we can't really measure the concentration of the molecule that leads to MAF, we cannot really acquire a more quantitative metric of MAF TPEF efficiency. Four fields from each of the four CAVD and three bone samples were imaged before and after EDTA treatment.

Imaging of Genetic Mouse Model

Three male apolipoprotein E knockout mouse hearts (ApoE−/−, age 10 months, on a C57BL/6 background, Jackson Laboratory, Bar Harbor, ME) and three, 2 month old female wild type (WT) mouse hearts (C57BL/6 mice, Jackson Laboratory, Bar Harbor, ME) were donated by the Jaffe Lab at Tufts Medical Center. The hearts were stored in 1× PBS during transport, valve isolation and imaging, which occurred within 24 hours from mouse sacrifice. The ApoE−/− mice were fed a high fat diet for 9 weeks before being sacrificed. This model has been previously shown to induce heart valve calcification as measured by von Kossa[53] and alkaline phosphatase-positive staining.[79] TPEF image stacks were acquired at 460 ± 20 nm and 525 ± 25 nm from two distinct regions of the aortic valve of each mouse using the Leica TCS SP2 microscope at an excitation of 800 nm. Each image stack consisted of 5 to 34 optical sections acquired with a step size of 5 μm. The relative MAF contribution

for each section was calculated and then averaged from all sections of a given image stack. MAF values for each of the six valves (three ApoE−/− and three WT valves) were calculated by averaging measurements from both Z stacks.

Coherent Anti-Stokes Raman Scattering (CARS) Microscopy with TPEF Imaging

CARS microscopy was performed using a dual output femtosecond pulsed laser system (Spectra-Physics Insight DeepSee, Santa Clara, CA, USA) and a customized confocal microscope (Olympus FV1000, Center Valley, PA, USA) using a 1.20 NA 60× water immersion objective (Olympus UPLSAPO 60XW, Center Valley, PA, USA). The fixed 1040 nm laser output was used as the Stokes beam while the widely tuneable output was set to 758 nm and used as the pump beam in order to probe the 3570 cm^{-1} vibrational band of OH^- in hydroxyapatite. A coherent anti-Stokes signal was thus generated at 596 nm, detected in the epi-direction using a photomultiplier tube (Hamamatsu H7422P-50, Hamamatsu City, Japan). A 750 nm shortpass filter was used to remove any residual excitation light (Chroma ET750SP-2P8, Bellows Falls, VT, USA), followed by a bandpass filter from 590 to 650 nm (Chroma HQ620/60M, Bellows Falls, VT, USA) To control laser power, a half-wave plate and a Glan-Laser polarizer were placed in front of each laser output port, and total incident power at the sample was maintained below 50 mW for all experimental conditions.

TPEF microscopy was performed using the same system as described above for CARS imaging. In this scenario however, the TPEF signal was generated by setting the tuneable output to 800 nm, where the fluorescence signals were collected in the epi-direction using a pair of thermoelectrically cooled photomultiplier tubes (Hamamatsu H7422P-40 and H7422P-50, Hamamatsu City, Japan). The fluorescence signal was first filtered using a 750 nm shortpass filter to remove any residual excitation light (Chroma ET750sp-2p8, Bellows Falls, VT, USA). The signal was then incident on a 480 nm dichroic mirror, where reflected shorter wavelengths were filtered once more through a bandpass filter (Chroma HQ475/60M, Bellows Falls, VT, USA) such that the effective fluorescence detection ranged from 445 to 480 nm; transmitted longer wavelengths were filtered through a separate bandpass filter (Chroma HQ525/50M, Bellows Falls, VT, USA) for detection ranging from 500 to 550 nm.

Time Lapse Imaging and MAF Quantification

PAAM gels were created, as described above on the activated glass of a 35 mm MatTek glass bottom dish (Ashland, MA). VICs were seeded at 100,000 cells/mm^2 and dosed with 1.25 ng/mL TGF-β_1 for 24 hours in an incubator at 37°C with 5% CO_2 before being cultured for 4 additional days in normal culture medium. The dish was then moved to the Leica TCS SP2 microscope and incubated using similar culture conditions for the duration of the experiment. TPEF images were acquired at 460 ± 20 nm and 525 ± 25 nm emission channels using 800 nm excitation and a 20×/0.7 NA air objective. A Z stack of 19 images, using the same imaging parameters for the duration of the experiment, was taken for a single field of view every 8 hours for 120 hours.

Following acquisition, images from each channel were processed to extract the related MAF contribution images. For each time point, the MAF image stacks were integrated along the Z

direction to create a 2D projection. The Template Matching and Slice Alignment ImageJ plugin was then used to align the 2D projections so that individual nodules could be tracked over time. For each time point, the 2D projection was then analyzed to examine individual nodules. Regions of interest (ROIs) were selected around mineralized nodules and a second integration along the × direction was performed for each time point. This led to a 1D intensity plot for each nodule that was used to calculate the full width at half maximum (FWHM), which related to the size of the nodules, and the integral, which represented the volumetric MAF nodule intensity. Four nodules, or ROIs, were analyzed for this study.

Statistical Analysis

One-way ANOVA with post hoc Tukey HSD tests were used to evaluate the differences between the human CAVD valves and rat bone before and after EDTA treatment using either the ratio of component 1 to component 2 (Figure 4) or the calculated MAF (Figure 5). Normality of the sample set was confirmed using the Shapiro-Wilk test, and equal variance was confirmed using the Brown-Forsythe test. A two-tailed, paired student T-test, confirmed with the same normality and variance testing, was used to determine significant differences between the ApoE−/− and wild type mice. No animal randomization was used for this study and the study was not blinded. As this type of optical characterization has not been done before, we could not perform rigorous a-priori calculations to estimate the sample size needed to detect significant differences. A two-tailed, paired student T-test was used to compare the mean MAF to collagen TPEF intensity ratio for CAVD and bone samples before and after EDTA treatment. Normality (Shapiro-Wilk) and equal variance (Brown-Forsythe) were also confirmed prior to implementing the statistical analysis. EDTA treatment experiments were done one time with replicates of four and three for the human CAVD valves and rat bones, respectively. The time lapse experiment was performed on one PAAM gel.

Supplementary Material

Refer to Web version on PubMed Central for supplementary material.

Acknowledgments

The authors are grateful to Marina Freytsis for her help in collecting the human CAVD valve samples at Tufts Medical Center and to the Jaffe Lab for their generous donation of freshly isolated ApoE−/− and wild type mouse hearts.

References

1. Mohler ER, et al. Bone Formation and Inflammation in Cardiac Valves. Circulation. 2001; 103:1522–1528. [PubMed: 11257079]
2. Nkomo VT, et al. Burden of valvular heart diseases: a population-based study. The Lancet. 2006; 368:1005–1011.
3. Freeman RV, Otto CM. Spectrum of calcific aortic valve disease: pathogenesis, disease progression, and treatment strategies. Circulation. 2005; 111:3316–3326. [PubMed: 15967862]
4. Rajamannan NM, et al. Calcific aortic valve disease: not simply a degenerative process: A review and agenda for research from the National Heart and Lung and Blood Institute Aortic Stenosis Working Group. Executive summary: Calcific aortic valve disease-2011 update. Circulation. 2011; 124:1783–1791. [PubMed: 22007101]

5. Sider KL, Blaser MC, Simmons CA. Animal models of calcific aortic valve disease. International journal of inflammation. 2011; 2011
6. Wexler L, et al. Coronary Artery Calcification: Pathophysiology, Epidemiology, Imaging Methods, and Clinical Implications: A Statement for Health Professionals From the American Heart Association. Circulation. 1996; 94:1175–1192. [PubMed: 8790070]
7. Linefsky, J., Otto, C. Ultrasound Imaging of Calcific Aortic Valve Disease. In: Aikawa, E., editor. Cardiovascular Imaging. Springer International Publishing; 2015. p. 225-249.
8. Fuster V, et al. Atherothrombosis and High-Risk Plaque: Part II: Approaches by Noninvasive Computed Tomographic/Magnetic Resonance Imaging. Journal of the American College of Cardiology. 2005; 46:1209–1218. [PubMed: 16198833]
9. New SEP, Aikawa E. Molecular Imaging Insights into Early Inflammatory Stages of Arterial and Aortic Valve Calcification. Circulation research. 2011; 108:1381–1391. [PubMed: 21617135]
10. Konig K, Schenke-Layland K, Riemann I, Stock UA. Multiphoton autofluorescence imaging of intratissue elastic fibers. Biomaterials. 2005; 26:495–500. [PubMed: 15276357]
11. Alavi SH, Ruiz V, Krasieva T, Botvinick EL, Kheradvar A. Characterizing the collagen fiber orientation in pericardial leaflets under mechanical loading conditions. Ann Biomed Eng. 2013; 41:547–561. [PubMed: 23180029]
12. Gerson CJ, Goldstein S, Heacox AE. Retained structural integrity of collagen and elastin within cryopreserved human heart valve tissue as detected by two-photon laser scanning confocal microscopy. Cryobiology. 2009; 59:171–179. [PubMed: 19591817]
13. Dweck M, et al. 18F-SODIUM FLUORIDE IS A MARKER OF ACTIVE CALCIFICATION AND DISEASE PROGRESSION IN PATIENTS WITH AORTIC STENOSIS. Journal of the American College of Cardiology. 2013; 61:E836.
14. Dweck MR, et al. Assessment of valvular calcification and inflammation by positron emission tomography in patients with aortic stenosis. Circulation. 2011 CIRCULATIONAHA. 111.051052.
15. Jenkins WS, et al. Valvular 18F-Fluoride and 18F-Fluorodeoxyglucose Uptake Predict Disease Progression and Clinical Outcome in Patients With Aortic Stenosis. Journal of the American College of Cardiology. 2015; 66:1200–1201. [PubMed: 26338001]
16. Vesey, A., Dweck, M., Newby, D. PET/CT Imaging of Inflammation and Calcification in CAVD: Clinical Studies. In: Aikawa, E., editor. Cardiovascular Imaging. Springer International Publishing; 2015. p. 201-223.
17. Ballyns JJ, Bonassar LJ. Image-guided tissue engineering. Journal of cellular and molecular medicine. 2009; 13:1428–1436. [PubMed: 19583811]
18. Feuchtner G. Imaging of cardiac valves by computed tomography. Scientifica. 2013; 2013
19. Goo HW. CT Radiation Dose Optimization and Estimation: an Update for Radiologists. Korean J Radiol. 2012; 13:1–11. [PubMed: 22247630]
20. Hjortnaes J, et al. Arterial and aortic valve calcification inversely correlates with osteoporotic bone remodelling: a role for inflammation. European heart journal. 2010; 31:1975–1984. [PubMed: 20601388]
21. Jaffer FA, Libby P, Weissleder R. Optical and Multimodality Molecular Imaging: Insights Into Atherosclerosis. Arteriosclerosis, Thrombosis, and Vascular Biology. 2009; 29:1017–1024.
22. Kherlopian A, et al. A review of imaging techniques for systems biology. BMC Systems Biology. 2008; 2:74. [PubMed: 18700030]
23. Hutson HN, et al. Calcific Aortic Valve Disease Is Associated with Layer-Specific Alterations in Collagen Architecture. PLoS One. 2016; 11:e0163858. [PubMed: 27685946]
24. Bertazzo S, et al. Nano-analytical electron microscopy reveals fundamental insights into human cardiovascular tissue calcification. Nat Mater. 2013; 12:576–583. [PubMed: 23603848]
25. Williams RM, Zipfel WR, Webb WW. Multiphoton microscopy in biological research. Current Opinion in Chemical Biology. 2001; 5:603–608. [PubMed: 11578936]
26. Georgakoudi I, Quinn KP. Optical imaging using endogenous contrast to assess metabolic state. Annu Rev Biomed Eng. 2012; 14:351–367. [PubMed: 22607264]
27. So PT, Dong CY, Masters BR, Berland KM. Two-photon excitation fluorescence microscopy. Annu Rev Biomed Eng. 2000; 2:399–429. [PubMed: 11701518]

28. Zipfel WR, et al. Live tissue intrinsic emission microscopy using multiphoton-excited native fluorescence and second harmonic generation. Proceedings of the National Academy of Sciences. 2003; 100:7075–7080.
29. Cui JZ, et al. Quantification of aortic and cutaneous elastin and collagen morphology in Marfan syndrome by multiphoton microscopy. Journal of Structural Biology. 2014; 187:242–253. [PubMed: 25086405]
30. König K, Schenke-Layland K, Riemann I, Stock U. Multiphoton autofluorescence imaging of intratissue elastic fibers. Biomaterials. 2005; 26:495–500. [PubMed: 15276357]
31. Fitzmaurice M, et al. Argon ion laser-excited autofluorescence in normal and atherosclerotic aorta and coronary arteries: Morphologic studies. American Heart Journal. 1989; 118:1028–1038. [PubMed: 2816687]
32. Benninger RK, Piston DW. Two-photon excitation microscopy for the study of living cells and tissues. Current protocols in cell biology. 2013 4.11 11–14.11. 24.
33. Huang S, Heikal AA, Webb WW. Two-photon fluorescence spectroscopy and microscopy of NAD(P)H and flavoprotein. Biophys J. 2002; 82:2811–2825. [PubMed: 11964266]
34. Croce A, Bottiroli G. Autofluorescence spectroscopy and imaging: a tool for biomedical research and diagnosis. European Journal of Histochemistry. 2014; 58
35. Perry SW, Burke RM, Brown EB. Two-photon and second harmonic microscopy in clinical and translational cancer research. Annals of biomedical engineering. 2012; 40:277–291. [PubMed: 22258888]
36. Chen X, Nadiarynkh O, Plotnikov S, Campagnola PJ. Second harmonic generation microscopy for quantitative analysis of collagen fibrillar structure. Nature protocols. 2012; 7:654. [PubMed: 22402635]
37. Cicchi R, et al. Scoring of collagen organization in healthy and diseased human dermis by multiphoton microscopy. Journal of Biophotonics. 2010; 3:34–43. [PubMed: 19771581]
38. Williams RM, Zipfel WR, Webb WW. Interpreting second-harmonic generation images of collagen I fibrils. Biophys J. 2005; 88:1377–1386. [PubMed: 15533922]
39. Campagnola PJ, Loew LM. Second-harmonic imaging microscopy for visualizing biomolecular arrays in cells, tissues and organisms. Nature biotechnology. 2003; 21:1356–1360.
40. Liu Z, et al. Rapid three-dimensional quantification of voxel-wise collagen fiber orientation. Biomedical optics express. 2015; 6:2294–2310. [PubMed: 26203362]
41. Liu Z, et al. Automated quantification of three-dimensional organization of fiber-like structures in biological tissues. Biomaterials. 2017; 116:34–47. [PubMed: 27914265]
42. Zoumi A, Yeh A, Tromberg BJ. Imaging cells and extracellular matrix in vivo by using second-harmonic generation and two-photon excited fluorescence. Proceedings of the National Academy of Sciences of the United States of America. 2002; 99:11014–11019. [PubMed: 12177437]
43. Richards-Kortum R, Sevick-Muraca E. Quantitative optical spectroscopy for tissue diagnosis. Annu Rev Phys Chem. 1996; 47:555–606. [PubMed: 8930102]
44. Cho A, Suzuki S, Hatakeyama J, Haruyama N, Kulkarni AB. A Method for Rapid Demineralization of Teeth and Bones. The Open Dentistry Journal. 2010; 4:223–229. [PubMed: 21339898]
45. Berzina-Cimdina, L., Borodajenko, N. Infrared Spectroscopy-Materials Science, Engineering and Technology. InTech; 2012. Research of calcium phosphates using Fourier transform infrared spectroscopy.
46. Ko ACT, et al. Multimodal nonlinear optical imaging of atherosclerotic plaque development in myocardial infarction-prone rabbits. BIOMEDO. 2010; 15:020501-020501–020503.
47. Verbunt RJAM, et al. Characterization of ultraviolet laser-induced autofluorescence of ceroid deposits and other structures in atherosclerotic plaques as a potential diagnostic for laser angiosurgery. American Heart Journal. 1992; 123:208–216. [PubMed: 1729827]
48. Le TT, Langohr IM, Locker MJ, Sturek M, Cheng J-X. Label-free molecular imaging of atherosclerotic lesions using multimodal nonlinear optical microscopy. BIOMEDO. 2007; 12:054007-054007–054010.

49. Wang, YL., Pelham, RJ, Jr. [39] Preparation of a flexible, porous polyacrylamide substrate for mechanical studies of cultured cells. In: Richard, BV., editor. Methods in Enzymology. Vol. 298. Academic Press; 1998. p. 489-496.
50. O'Brien KD. Pathogenesis of calcific aortic valve disease: a disease process comes of age (and a good deal more). Arterioscler Thromb Vasc Biol. 2006; 26:1721–1728. [PubMed: 16709942]
51. Evans CL, Xie XS. Coherent anti-Stokes Raman scattering microscopy: chemical imaging for biology and medicine. Annu Rev Anal Chem. 2008; 1:883–909.
52. Sider KL, Blaser MC, Simmons CA. Animal Models of Calcific Aortic Valve Disease. International Journal of Inflammation. 2011; 2011:364310. [PubMed: 21826258]
53. Tanaka K, et al. Age-associated aortic stenosis in apolipoprotein E-deficient mice. J Am Coll Cardiol. 2005; 46:134–141. [PubMed: 15992647]
54. Hutcheson JD, Aikawa E, Merryman WD. Potential drug targets for calcific aortic valve disease. Nature reviews Cardiology. 2014; 11:218–231. [PubMed: 24445487]
55. Aikawa E, et al. Osteogenesis associates with inflammation in early-stage atherosclerosis evaluated by molecular imaging in vivo. Circulation. 2007; 116:2841–2850. [PubMed: 18040026]
56. Giachelli CM. Ectopic calcification. The American journal of pathology. 1999; 154:671–675. [PubMed: 10079244]
57. Richards-Kortum R, et al. Spectroscopic diagnosis of colonic dysplasia. Photochemistry and photobiology. 1991; 53:777–786. [PubMed: 1653427]
58. Guerraty M, Mohler ER. Models of aortic valve calcification. Journal of Investigative Medicine. 2007; 55:278–283. [PubMed: 17963676]
59. Hutcheson JD, et al. Genesis and growth of extracellular-vesicle-derived microcalcification in atherosclerotic plaques. Nature materials. 2016
60. Clark CR, Bowler MA, Snider JC, Merryman WD. Targeting Cadherin-11 Prevents Notch1-Mediated Calcific Aortic Valve Disease. Circulation. 2017; 135:2448–2450. [PubMed: 28606953]
61. Perosky JE, et al. Early detection of heterotopic ossification using near-infrared optical imaging reveals dynamic turnover and progression of mineralization following Achilles tenotomy and burn injury. Journal of Orthopaedic Research. 2014; 32:1416–1423. [PubMed: 25087685]
62. Zhang Y, et al. A compact fiber-optic SHG scanning endomicroscope and its application to visualize cervical remodeling during pregnancy. Proceedings of the National Academy of Sciences of the United States of America. 2012; 109:12878–12883. [PubMed: 22826263]
63. Murari K, et al. Compensation-free, all-fiber-optic, two-photon endomicroscopy at 1.55 μm. Optics letters. 2011; 36:1299–1301. [PubMed: 21479064]
64. Nishimura R, et al. 2014 AHA/ACC guideline for the management of patients with valvular heart disease: executive summary: a report of the American College of Cardiology/American Heart Association Task Force on Practice Guidelines. J Am Coll Cardiol. 2014; 63:2438–88. [PubMed: 24603192] Correction. Journal of the American College of Cardiology. 2014; 63
65. Mathieu P, et al. The pathology and pathobiology of bicuspid aortic valve: state of the art and novel research perspectives. The Journal of Pathology: Clinical Research. 2015; 1:195–206. [PubMed: 27499904]
66. Sethuraman S, Amirian JH, Litovsky SH, Smalling RW, Emelianov SY. Spectroscopic intravascular photoacoustic imaging to differentiate atherosclerotic plaques. Optics express. 2008; 16:3362–3367. [PubMed: 18542427]
67. Wang B, et al. Intravascular Photoacoustic Imaging. IEEE journal of quantum electronics. 2010; 16:588–599. [PubMed: 21359138]
68. Fu HL, et al. Flexible miniature compound lens design for high-resolution optical coherence tomography balloon imaging catheter. J Biomed Opt. 2008; 13:060502. [PubMed: 19123643]
69. Hassan T, Piton N, Lachkar S, Salaun M, Thiberville L. A Novel Method for In Vivo Imaging of Solitary Lung Nodules Using Navigational Bronchoscopy and Confocal Laser Microendoscopy. Lung. 2015; 193:773–778. [PubMed: 26216723]
70. Achenbach S, et al. Detection of calcified and noncalcified coronary atherosclerotic plaque by contrast-enhanced, submillimeter multidetector spiral computed tomography: a segment-based comparison with intravascular ultrasound. Circulation. 2004; 109:14–17. [PubMed: 14691045]

71. Radi MJ. Calcium oxalate crystals in breast biopsies. An overlooked form of microcalcification associated with benign breast disease. Arch Pathol Lab Med. 1989; 113:1367–1369. [PubMed: 2589947]

72. Sullivan K, Quinn K, Tang K, Georgakoudi I, Black L III. Extracellular matrix remodeling following myocardial infarction influences the therapeutic potential of mesenchymal stem cells. Stem Cell Res Ther. 2014; 5:1–16. [PubMed: 24405778]

73. Quinlan AM, Billiar KL. Investigating the role of substrate stiffness in the persistence of valvular interstitial cell activation. Journal of biomedical materials research Part A. 2012; 100:2474–2482. [PubMed: 22581728]

74. Liao PS, Chen TS, Chung PC. A fast algorithm for multilevel thresholding. J Inf Sci Eng. 2001; 17:713–727.

75. Levitt JM, et al. Diagnostic cellular organization features extracted from autofluorescence images. Optics letters. 2007; 32:3305–3307. [PubMed: 18026288]

76. Xylas J, Alt-Holland A, Garlick J, Hunter M, Georgakoudi I. Intrinsic optical biomarkers associated with the invasive potential of tumor cells in engineered tissue models. Biomedical optics express. 2010; 1:1387–1400. [PubMed: 21258557]

77. Xylas J, et al. Noninvasive assessment of mitochondrial organization in three-dimensional tissues reveals changes associated with cancer development. Int J Cancer. 2015; 136:322–332. [PubMed: 24862444]

78. Pouli D, et al. Imaging mitochondrial dynamics in human skin reveals depth-dependent hypoxia and malignant potential for diagnosis. Sci Transl Med. 2016; 8:367ra169.

79. Zeadin M, et al. Effect of leptin on vascular calcification in apolipoprotein E–deficient mice. Arteriosclerosis, thrombosis, and vascular biology. 2009; 29:2069–2075.

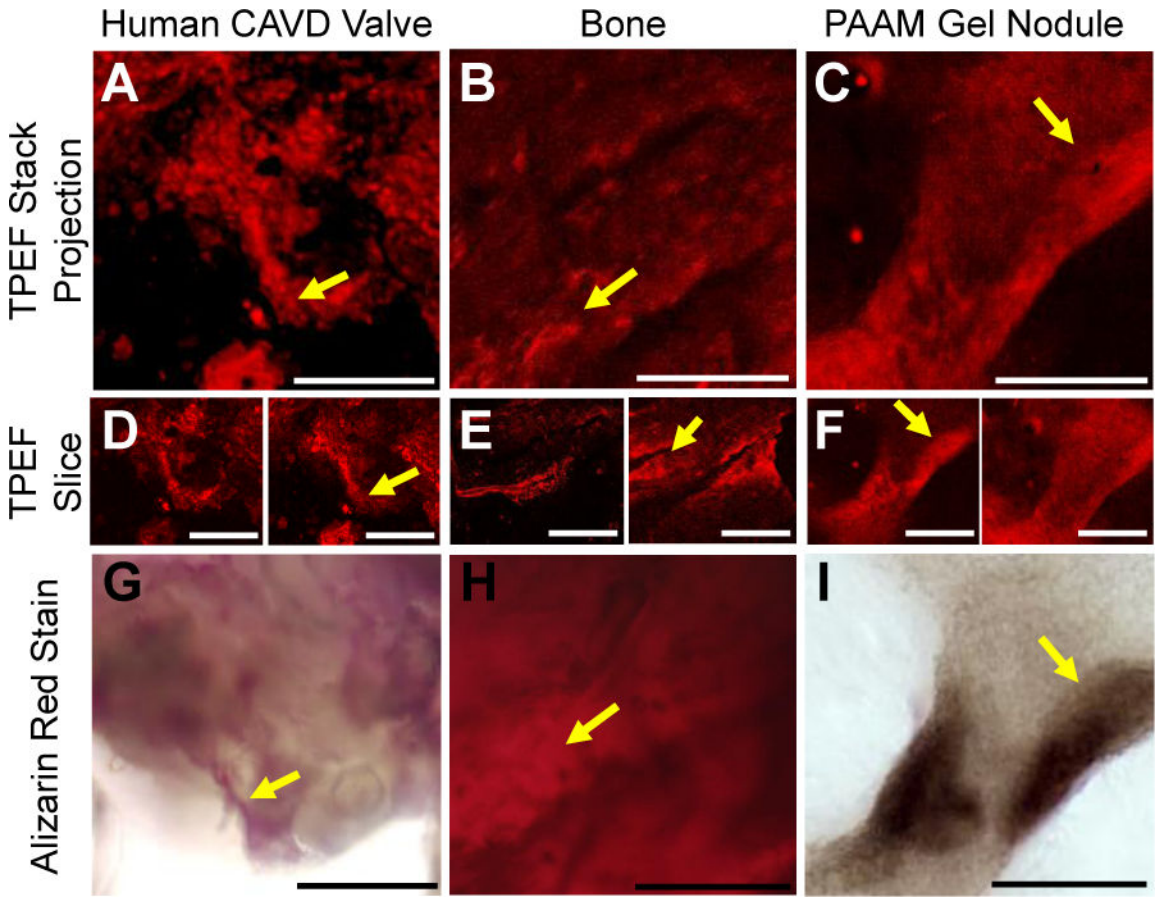

Figure 1.

Visual analysis of TPEF images compared to Alizarin Red staining of a human CAVD nodule, a rat bone, and a PAAM gel grown nodule. Two-photon excited autofluorescence and Alizarin Red staining for mineralization within CAVD human valves (A, D, G), rat bone (B, E, H) and nodules grown on PAAM gels seeded with rat VICs (C, F, I). Projections of TPEF image volumes (A, B, C) were created by averaging individual depth-resolved optical sections (D, E, F). The endogenous TPEF patterns are consistent with the spatial distribution of subsequent Alizarin Red staining of the same region (G, H, I). Yellow arrows show features similar between the TPEF and Alizarin Red images. Scale bars are 50 μm.

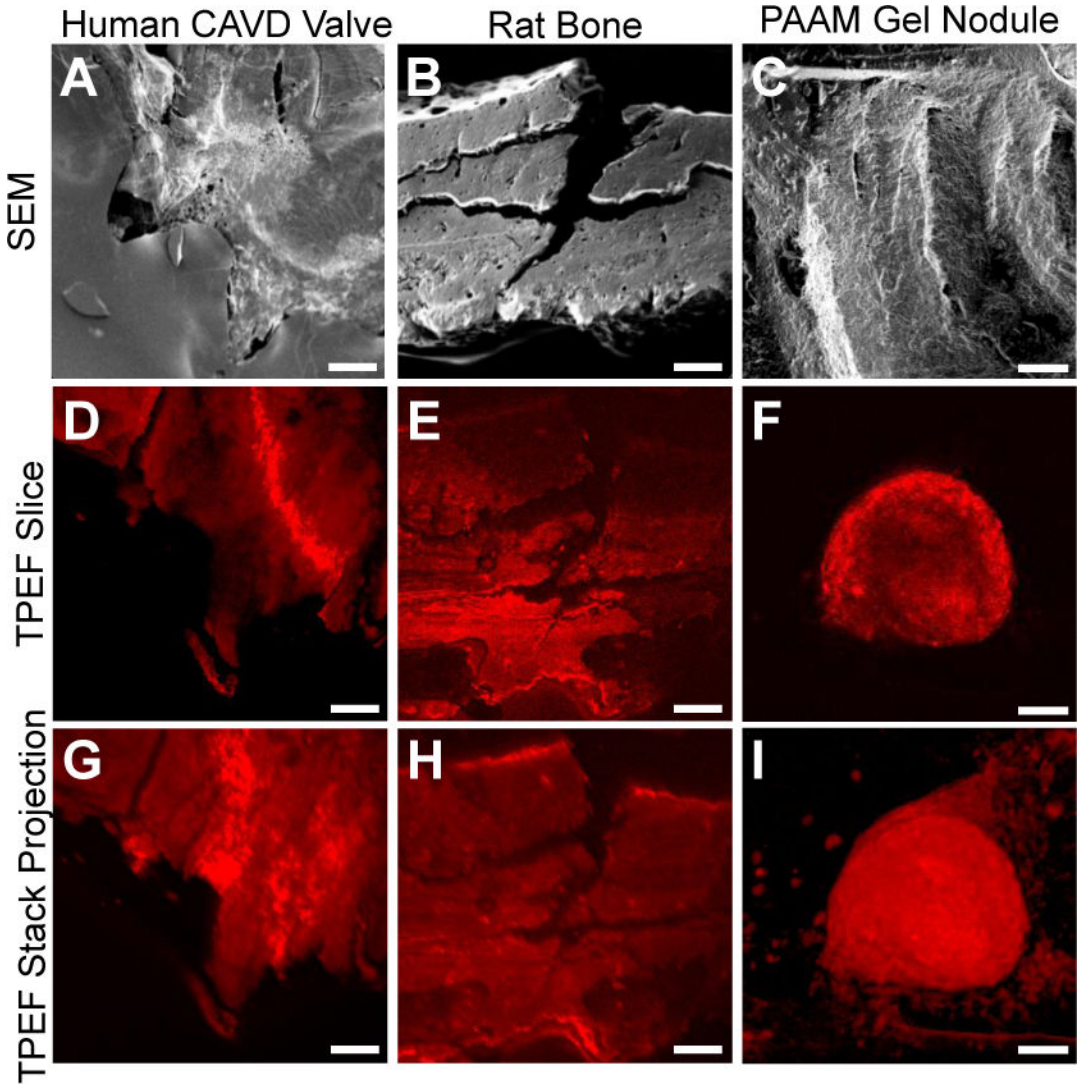

Figure 2.

Representative images of human CAVD nodules, rat bone samples, and PAAM gel nodules taken using SEM and TPEF. SEM images of nodules from a human CAVD valve (A), rat bone (B) and PAAM gels (C) show the topography of the different types of calcific nodules. Representative TPEF slices (D, E, F) and intensity projections of the image volumes (G, H, I) also demonstrate the ability to identify textural patterns between calcified samples. Scale bars are 100 μm.

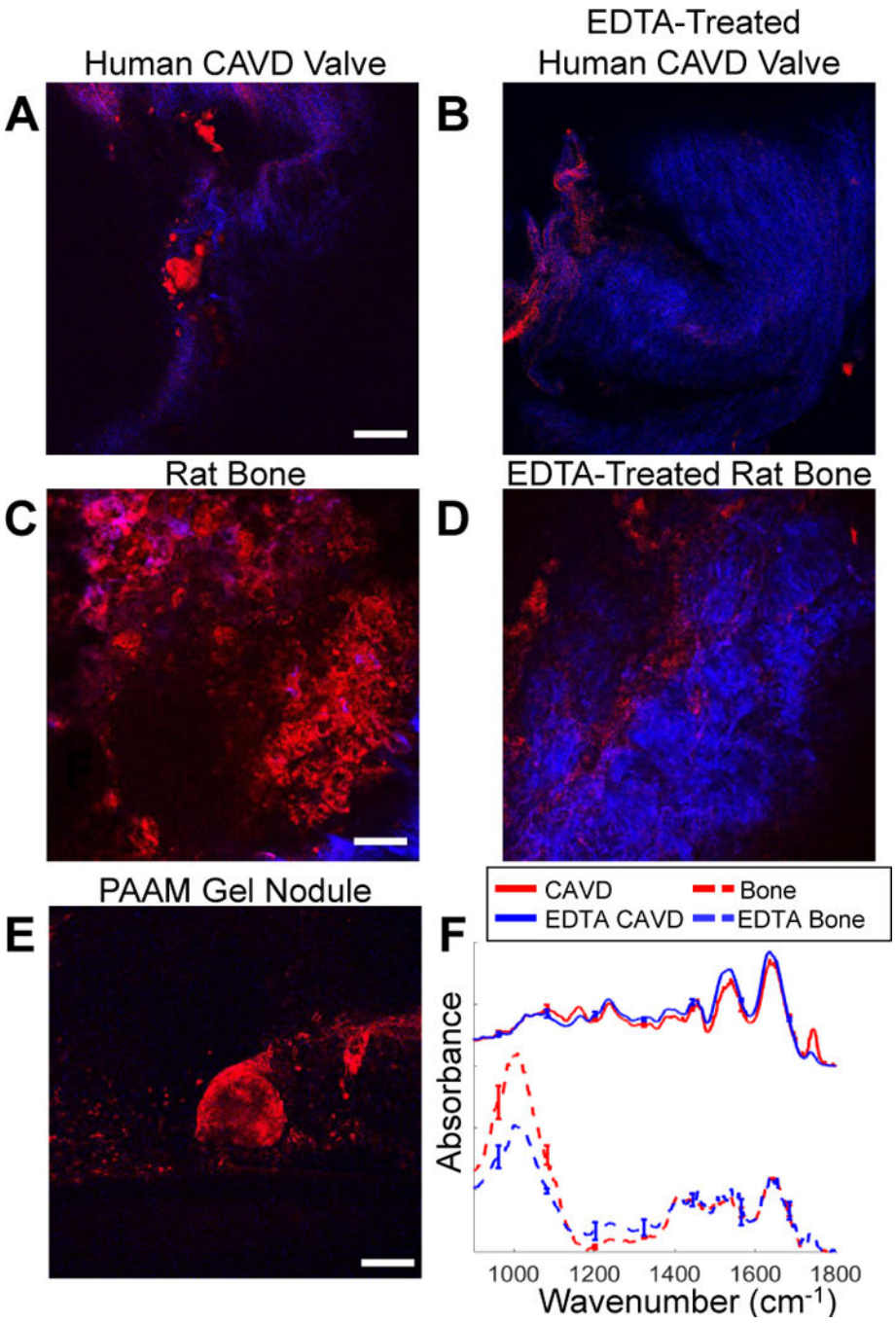

Figure 3.

Effect of EDTA treatment on endogenous TPEF. Representative optical sections of a human CAVD valve before (A) and after (B) EDTA treatment, as well as rat tibia bone before (C) and after (D) EDTA treatment suggest that 525nm TPEF emission (red) is associated with mineralization. Collagen SHG (blue) is not attenuated by EDTA treatment. No collagen SHG is observed in PAAM gels (E). FT-IR spectra taken before and after EDTA treatment for the CAVD (F) and bone (G) samples show changes in absorbance with loss of mineralization. Scale bars are 100 μm. Error bars show standard error of mean.

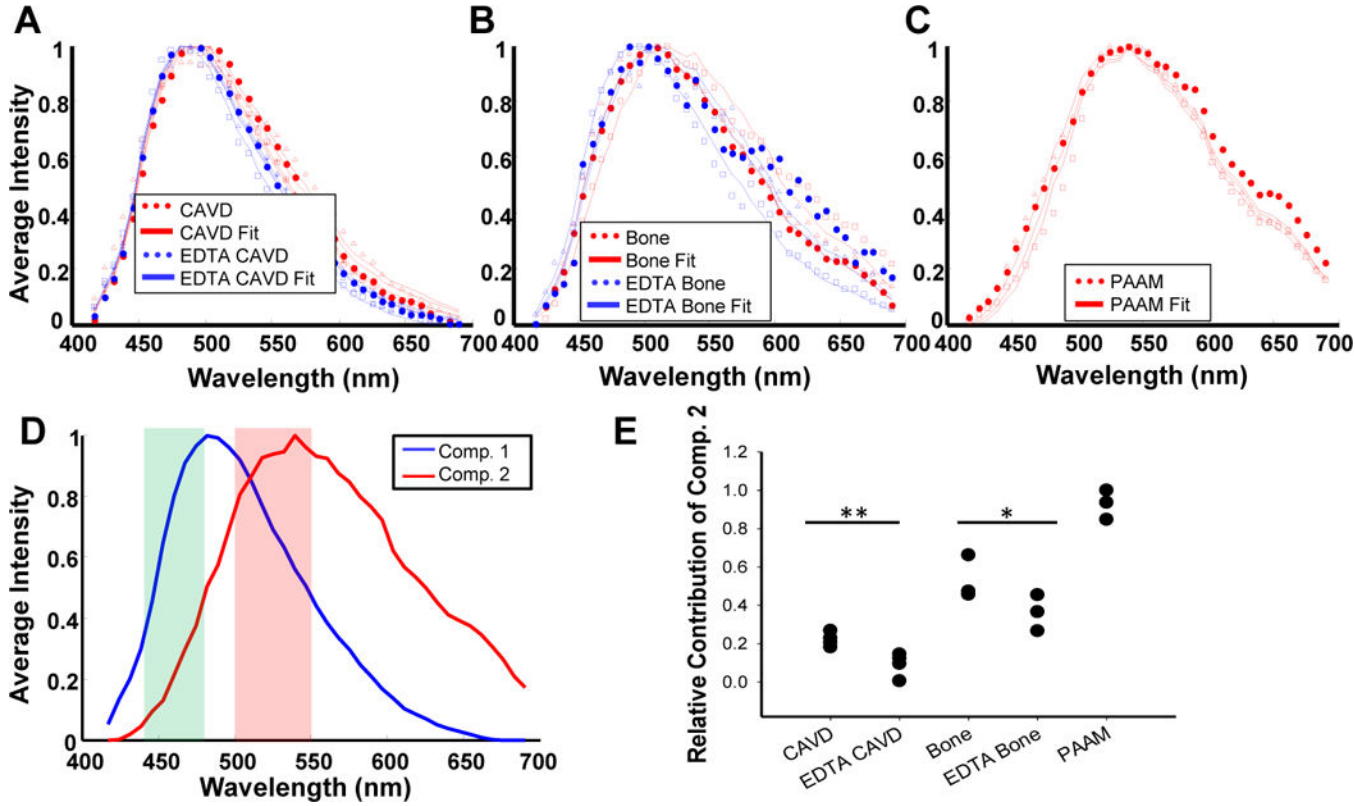

Figure 4.

Analysis of TPEF emission spectra reveals emission spectrum of mineralization associated fluorescence. Representative TPEF emission spectra of (A) human CAVD valves before and after EDTA treatment, (B) rat bone before and after EDTA treatment, and (C) nodules grown on PAAM gels indicate a blue shift with EDTA treatment. For A-C, representaive data sets are delineated using either triangles, squares, or dots; representiave fits are shown using a solid line. Spectral unmixing through non-negative matrix factorization indicated two spectral components (D), which provided a good fit to the data in A-C. Shaded regions in (D) represent the emission filter bands employed in TPEF imaging. (E) The relative contribution of component 2 derived from spectral unmixing and associated with mineralization is reduced upon EDTA treatment (*P=0.088, **P<0.001 based on ANOVA and post-hoc Tukey test). Averaged spectra are shown from 4 CAVD valves, 4 CAVD EDTA valves, 3 bone samples, 3 EDTA bone samples, and 3 PAAM gel nodules.

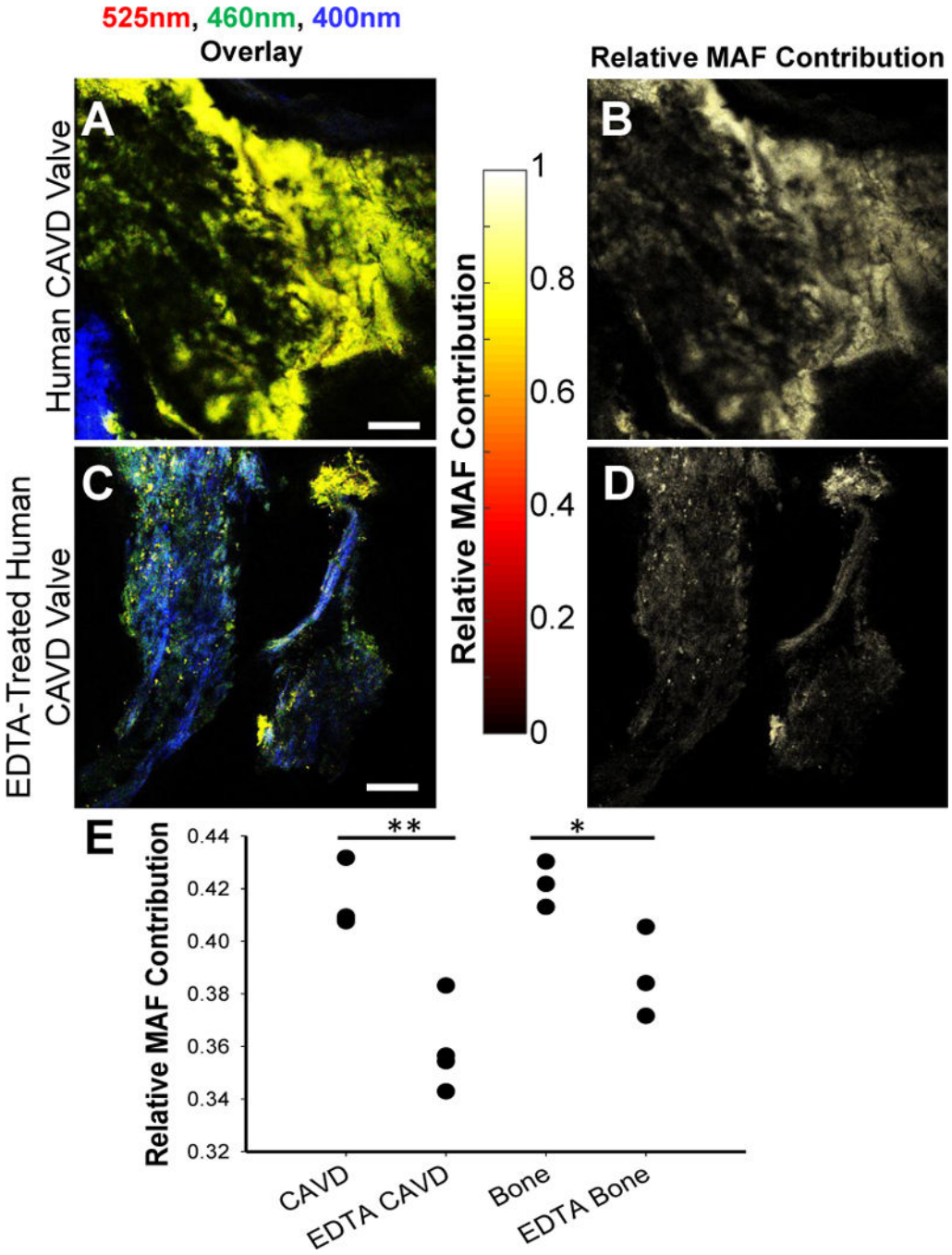

Figure 5.

MAF images enable enhanced visualization of mineralized sample regions. Human CAVD valve (A) intensity overlay of 525nm TPEF (red), 460nm TPEF (green), and SHG (blue), as well as (B) calculated MAF images. EDTA treatment causes an overall reduction in TPEF intensity (C) and a reduction in the relative 525nm emission resulting in a lower MAF contribution (D). The relative MAF contribution (E) is significantly decreased with EDTA treatment to remove calcification (*P=0.002; **P=0.045 based on ANOVA and post-hoc

Tukey Test). Data is shown from 4 CAVD and CAVD EDTA samples and 3 bone and EDTA bone samples. Scale bar is 100 μm.

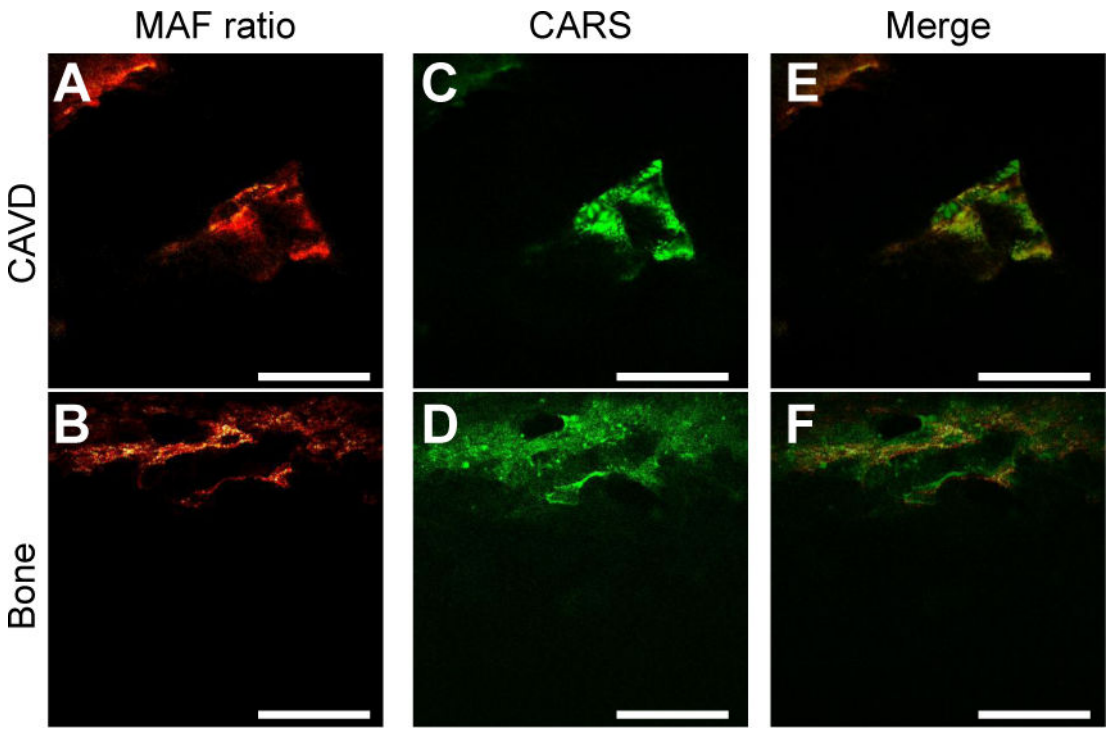

Figure 6.

MAF signal overlaps with CARS images. TPEF images taken on a an Olympus FX1000 with CARS imaging with CARS imaging capabilities were used to calculate the MAF for CAVD valves (A) and bone (B) samples. Corresponding CARS images of the same fields were taken (C,D) and merged (E,F). Scale bars are 100 μm.

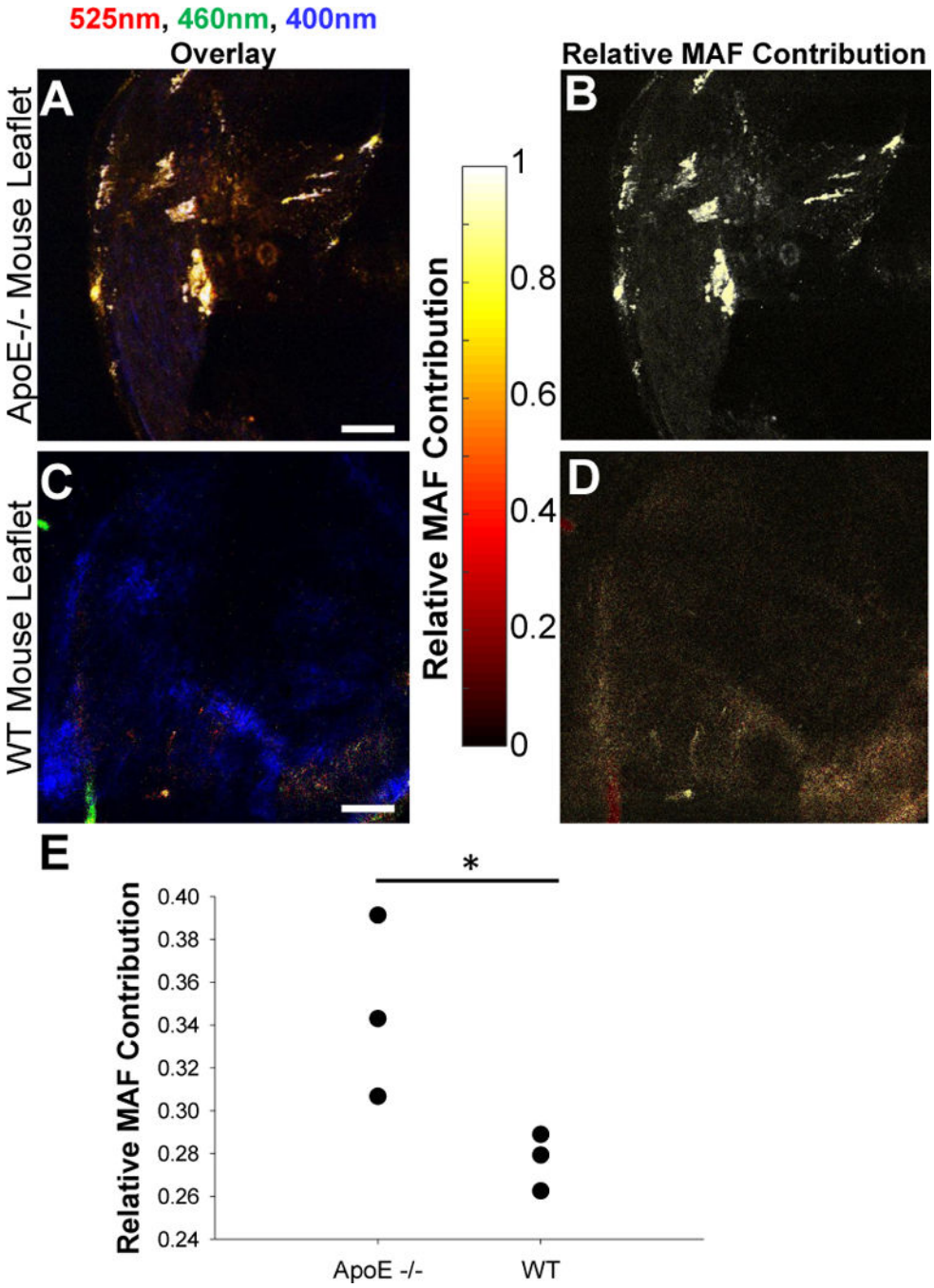

Figure 7.

An ApoE−/− mouse model confirms the use of the MAF as a quantifiable metric for calcification. TPEF imaging of aortic valves from aged ApoE−/− mice with an (A) intensity overlay of 525nm TPEF (red), 460nm TPEF (green), and SHG (blue), as well as (B) the calculated MAF concentration highlights distinct calcified nodules relative to wild type mice (C, D). The relative contribution of the MAF (E) is significantly increased in ApoE−/− mouse valves (P=0.0525). Data is shown for 3 ApoE−/− valves and 3 WT valves. Scale bar is 100 μm.

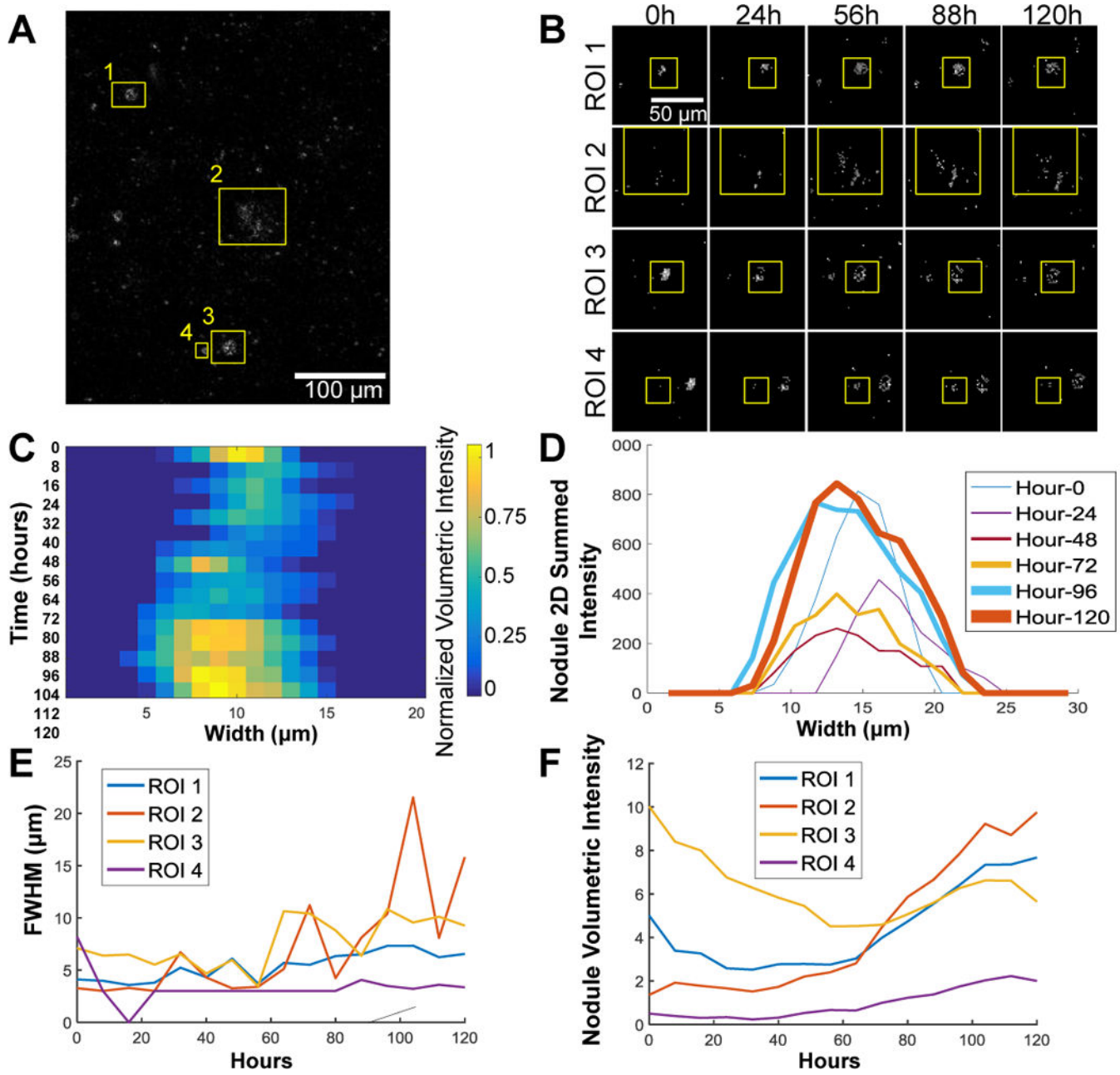

Figure 8.

Time lapse experiment of calcification on PAAM gels shows measured change in nodule size. (A) The 525nm/460nm image ratio at time zero of a 120 hour time lapse experiment showing 4 regions of interest (ROIs) used for analysis. (B) Representative time points of each ROI showing the regions that were analyzed. After taking the summed 3D projections and the 525nm/460nm ratio and calculating the MAF contribution, the sum along the image plane can be used to find the nodule volumetric intensity shown for the image stacks (B) and the individual line plots for the nodule volume over time (C). These images were then used

to calculate the full with at half maximum (FWHM; E) and the area under the curve of the intensity profile of the 3D summed projections, or the volumetric intensity (F).